American Mineralogist, Volume 108, pages 1530–1537, 2023

Thermal equation of state of ice-VII revisited by single-crystal X-ray diffraction

Xiaojing Lai[1,2,*], Feng Zhu[3], Dongzhou Zhang[2], Sergey Tkachev[4], Vitali B. Prakapenka[4], Keng-Hsien Chao[2], and Bin Chen[2]

[1]Gemmological Institute, State Key Laboratory of Geological Processes and Mineral Resources, China University of Geosciences, Wuhan, Hubei, 430074, China
[2]Hawaii Institute of Geophysics and Planetology, University of Hawai'i at Mānoa, Honolulu, Hawaii 96822, U.S.A.
[3]School of Earth Sciences, State Key Laboratory of Geological Processes and Mineral Resources, China University of Geosciences, Wuhan, Hubei, 430074, China
[4]Center for Advanced Radiation Sources, University of Chicago, Chicago, Illinois 60637, U.S.A.

Abstract

Ice-VII is a high-pressure polymorph of H_2O ice and an important mineral widely present in many planetary environments, such as in the interiors of large icy planetary bodies, within some cold subducted slabs, and in diamonds of deep origin as mineral inclusions. However, its stability at high pressures and high temperatures and thermoelastic properties are still under debate. In this study, we synthesized ice-VII single crystals in externally heated diamond-anvil cells and conducted single-crystal X-ray diffraction experiments up to 78 GPa and 1000 K to revisit the high-pressure and high-temperature phase stability and thermoelastic properties of ice-VII. No obvious unit-cell volume discontinuity or strain anomaly of the high-pressure ice was observed up to the highest achieved pressures and temperatures. The volume-pressure-temperature data were fitted to a high-temperature Birch-Murnaghan equation of state formalism, yielding bulk modulus K_{T0} = 21.0(4) GPa, its first pressure derivative K'_{T0} = 4.45(6), dK/dT = –0.009(4) GPa/K, and thermal expansion relation $\alpha_T = 15(5) \times 10^{-5} + 15(8) \times 10^{-8} \times (T - 300)$ K^{-1}. The determined phase stability and thermoelastic properties of ice-VII can be used to model the inner structure of icy cosmic bodies. Combined with the thermoelastic properties of diamonds, we can reconstruct the isomeke P-T paths of ice-VII inclusions in diamond from depth, offering clues on the water-rich regions in Earth's deep mantle and the formation environments of those diamonds.

Keywords: High-pressure ice, diamond-anvil cell, thermal equation of state, icy planetary bodies, ice-VII diamond inclusions

Introduction

H_2O is an essential component for life on our habitable planet and is widely present in a large variety of planetary environments in our Solar System. It has a rich and intriguing phase diagram with at least 18 phases found to date (Futera et al. 2020), due to the coexistence of covalent and hydrogen bonds. The physics of high-pressure ices has attracted great interest from the perspective of condensed matter physics (Prakapenka et al. 2021; Sugimura et al. 2008). The physical properties of H_2O phases, as liquids or solids, are vital for modeling the internal structure of the icy satellites such as Jovian satellites Europa, Ganymede, Callisto (Kuskov and Kronrod 2001; Sohl et al. 2002), Saturn's satellite Titan (Tobie et al. 2005), and H_2O-rich exo-planets (Seager et al. 2007).

Ice-VII is a high-pressure polymorph of H_2O ice with a wide pressure stability field above 2.1 GPa at room temperature, which is therefore proposed to be present inside many icy planets and satellites (Huang et al. 2021; Poirier et al. 1981; Seager et al. 2007). Ice-VII was also suggested to exist in some cold slabs subducted to the deep Earth, which would contribute to the cycling of water in deep Earth and the occurrences of seismic activities at slab-mantle interfaces (Bina and Navrotsky 2000). Recently, ice-VII was identified as a mineral after its discovery as inclusions of superdeep diamonds (Tschauner et al. 2018). This finding indicates that H_2O phases/fluid such as ice-VII may exist as an independent phase in local water-rich regions in the deep Earth, and their thermoelastic properties would be essential to constrain the entrapment pressure or depth at which those superdeep diamonds were formed (Tschauner et al. 2018). Therefore, the high-pressure-temperature (P-T) properties of ice-VII are needed for modeling the internal structure, evolution, and dynamics of icy planetary bodies and for understanding the water cycle of the Earth.

The ice-VII was first reported in 1937 (Bridgman 1937) and its *bcc*-type O framework structure was determined by powder X-ray diffraction (XRD) method in 1964 (Kamb and Davis 1964). Its high-pressure structural behavior has been investigated by powder and single-crystal XRD as well as neutron diffraction at ambient temperature (Guthrie et al. 2013; Hemley et al. 1987; Loubeyre et al. 1999). The crystal structure of ice-VII consists of two interpenetrating, but not interconnecting anti-cristobalite sublattice shifted by (0.125, 0.125, 0.125) relative to each other. In ice-VII, each O atom is tetrahedrally linked to four nearest neighbor O atoms by hydrogen bonds (with two accepted O-H···O and two donated O···H-O bonds), and the hydrogen occupancy is disordered subject to the ice rules (Kamb and Davis 1964)

* E-mail: laixiaojing@cug.edu.cn

0003-004X/23/0008–1530$05.00/DOI: https://doi.org/10.2138/am-2022-8554

(Fig. 1). Besides ice-VII, there are two other high-pressure ices called ice VIII and ice X. These three high-pressure ices share a similar *bcc*-type O frame structure. Ice VIII can be obtained from the cooling of ice-VII to below 293 K (Brown and Whalley 1966; Kuhs et al. 1984). It has ordered hydrogen occupancy compared with ice-VII, which results in the elongation of the *c*-axis, changing its symmetry from cubic to tetragonal. Ice-VII is observed to gradually transform into ice X at high pressures (Aoki et al. 1996; Goncharov et al. 1999; Grande et al. 2022; Li et al. 2019; Meier et al. 2018; Shi et al. 2021; Song et al. 1999; Sugimura et al. 2008). The transition from ice-VII to ice X is a process called "hydrogen bond symmetrization," in which the O-H···O hydrogen bond transforms into a symmetric O-H-O bond. In contrast to ice-VII, the hydrogen in ice X becomes equidistant between the neighboring O atoms and the basic building block is no longer H_2O molecule, making ice X at least partially ionic.

The transition from ice-VII to dynamically disordered ice-VII (ice-VII′) and then to ice X was proposed according to Raman, infrared (IR), nuclear magnetic resonance (NMR), Brillouin studies, and first principle calculations (Aoki et al. 1996; Goncharov et al. 1999; Grande et al. 2022; Li et al. 2019; Meier et al. 2018; Shi et al. 2021; Song et al. 1999). However, the transition pressures are not consistent in these studies ranging from 31 to 75 GPa. Whether the transition from ice-VII to ice X can be observed by XRD also remains controversial (Asahara et al. 2010; Hemley et al. 1987; Sugimura et al. 2008; Wolanin et al. 1997). The XRD patterns of ice-VII and ice X are similar and volume discontinuity caused by this transition was not observed in some previous XRD results (Hemley et al. 1987; Wolanin et al. 1997) while in some other studies, an abnormal volume reduction was reported at 40–60 GPa (Asahara et al. 2010; Sugimura et al. 2008). A phase change from cubic to tetragonal structure of ice-VII was also reported in the range of 5.1–14 GPa as indicated by the splitting of (110) peaks in Somayazulu et al. (2008), (110), (200), (211), and (220) peaks in Kadobayashi et al. (2014) and (200) peak in Grande et al. (2022), respectively. In addition, Guthrie et al. (2013) found a kink in the ratio of the intensity of (220)/(110) peaks of ice-VII at 13 GPa using powder neutron diffraction, suggesting an interstitial proton model above 13 GPa. Iitaka et al. (2015) re-examined their model by theoretical calculation and X-ray Raman spectroscopy (XRS) and argues that the model cannot explain their XRS results of ice-VII above 13 GPa.

The high-*P*-*T* compressional behavior of ice-VII was only investigated using powder XRD method. Previous works have determined its thermal equation of state (EoS) up to 60 GPa and 850 K (Bezacier et al. 2014; Fei et al. 1993; Frank et al. 2004; Sugimura et al. 2010). These *P*-*V*-*T* data were further used to calculate the melting curve of ice-VII through relations of equilibrium thermodynamics and to examine the existing EoS of fluid H_2O (Fei et al. 1993; Frank et al. 2004; Sugimura et al. 2010). Due to the difficulty of growing single crystal of ice-VII in the diamond-anvil cell, there are barely any high-*P*-*T* single-crystal XRD studies on ice-VII. In this study, we synthesized single-crystal ice-VII without obvious lattice stress using an externally heated diamond-anvil cell (EHDAC). This allows us to carry out synchrotron-based single-crystal XRD experiments combined with EHDAC to obtain the crystal structure information of ice-VII at high-*P*-*T* conditions as well as its thermal EoS up to the highest pressure of 78 GPa and the highest temperature of 1000 K.

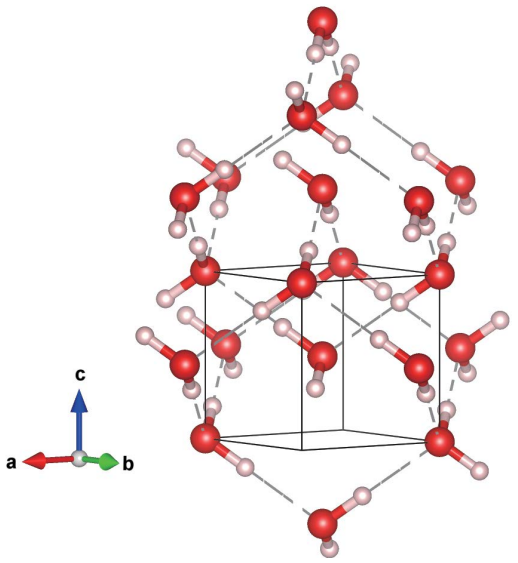

Figure 1. Crystal structure of ice-VII. Red spheres represent oxygen atoms, pink spheres represent hydrogen atoms, and dashed lines represent hydrogen bonds. The solid cube presents the unit-cell boundary of ice-VII (space group *Pnm*, $Z = 2$). Some atoms in the unit cell were hid to show a clear configuration of two interpenetrating, but not interconnecting anti-cristobalite sublattice. The arrangements of hydrogen atoms are illustrated obeying the ice rule. (Color online.)

Methods

Two BX90 DACs with 300 μm culet standard cut diamond anvils were used for the synthesis of ice-VII and single-crystal XRD experiments at high *P*-*T* conditions (Kantor et al. 2012). For each cell, two 60° opening tungsten carbide seats were used. A lab-fabricated heater using Pt-10 wt%Rh (0.01″) wires as the heating wires was utilized in the EHDAC (Lai et al. 2020). One K-type thermocouple (Chromega-Alomega 0.005″) was mounted near the diamond culet and in touch with the downstream diamond to measure the temperature. The rhenium gasket was pre-indented to a thickness of ~40 μm and a sample chamber of 120 μm in diameter was drilled by laser micro-drilling machine. A drop of deionized water (ultra-filtered, Fisher Scientific), two small ruby spheres as pressure calibrants during the single-crystal synthesis (Mao et al. 1986), and a piece of gold foil as the primary pressure scale in XRD experiments (Fei et al. 2007) were loaded in the sample chamber. Pressure calibration at high temperature used thermal EoS of gold (Fei et al. 2007), which relies on the temperature determination, so the uncertainty of temperature and the EoS parameters will also propagate to the pressure uncertainty.

The samples were compressed to above 2.1 GPa at room temperature and then ice-VII single crystals were synthesized through several cycles of heating and cooling using EHDACs (Lai et al. 2020). The diameter of the synthesized single-crystal ice-VII is about 100 μm (Online Materials[1] Fig. S1). Single-crystal XRD characterizations of the synthesized ice-VII and the high-*P*-*T* experiments were conducted at beamline 13-BMD, the Advanced Photon Source (APS), Argonne National Lab. The typical size of the focused monochromatic X-ray beam (λ = 0.3344 or 0. 2952 Å) was 4 × 8 μm^2. Pilatus 1M and Perkin Elmer flat panel detectors were used to collect the diffraction patterns. The X-ray accessible opening angles of the DACs were 39° and 40° for run-1 and run-2, respectively. Step scans were collected at 0.5 °/step, and the exposure time per step was 5 s. The investigated range of pressure was 3.5 to 78.2 GPa, and the range of the temperature was 300 to 1000 K. Temperature was controlled by modulating the voltage applied to the resistive heater. It took about 30 min in total for each data point, including the time for increasing and stabilizing temperature as well as for data collection. To protect diamond anvils and EHDAC components from oxidization and to reduce heat loss to the open air at high temperatures, a vacuum enclosure with cooling water was used

for the experiments after the XRD characterization of ice-VII at 3.5 GPa in run-2. The sample was then heated to multiple high temperatures up to 1000 K in run-2.

To analyze the synchrotron-based single-crystal XRD data, we utilized the ATREX software package (Dera et al. 2013) and Olex2 software (Dolomanov et al. 2009). Step scans were also merged into one XRD pattern, integrated by DIOPTAS software (Prescher and Prakapenka 2015). Lattice parameters were refined by PDindexer software (Seto 2010). The *P-V-T* data were fitted by the EoSFit7-GUI program (Gonzalez-Platas et al. 2016). The isomeke *P-T* paths of ice-VII in diamonds were calculated by the EoSFit7Pinc program (Angel et al. 2017).

Results and discussion

Crystal structure and phase stability of ice-VII

Most of previous studies synthesized ice-VII by cold compression of water. Through the solid-solid transition from ice-VI to ice-VII, the synthesized ice-VII is typically powder or polycrystalline. In this study, the synthesized large ice-VII single crystals, which grew from the melt, have little lattice stress as indicated by the sharp Bragg diffraction peaks in synchrotron-based single-crystal XRD images (Fig. 2a; Online Materials[1] Figs. S2 and S3). The available XRD data are indexed and consistent with $Pn\bar{3}m$ special extinctions, indicating that the synthesized ice-VII adopts a cubic lattice with space group $Pn\bar{3}m$ (Z = 2), with unit-cell parameters $a = b = c$ = 3.2510(10) Å at 5.5 GPa and 300 K in run-1 and $a = b = c$ = 3.3046(5) Å at 3.5 GPa in run-2. In run-1, the vector along DAC axis is determined to be (–0.105, 0.995, 0), indicating that the synthesized ice-VII single crystal was oriented nearly parallel to the crystal axis [010]/*b* axis with some tilt toward *a* axis along the X-ray beam. With a DAC of 39° opening angle, only one reciprocal plane was observed, and for the observed index of peaks, k is always 0 (Fig. 2). In run-2, the vector along DAC axis is (0.943, –0.199, 0.265). Because hydrogen atoms scatter X-ray very weakly at the energy used in the experiment and the DAC opening angle was limited, we could not reliably refine the position of the hydrogen atoms in the crystal structure and only oxygen was included for structure refinement. For those two data points at starting pressures (5.5 GPa in run-1 and 3.5 GPa in run-2), 21 and 20 reflections were refined, respectively, which gives the R_{int} factors of 13.28% and 7.3%. The refinements of 7 out of 21 and 8 out of 20 reflections gives an R1 factor of 6.3 and 6.69%, respectively, suggesting the structure is consistent with the cubic ice-VII (CIF in Online Materials[1]).

The XRD patterns of the high-quality single crystal became smeared after compression and heating due to quasi-hydrostatically conditions in DAC. The number of peaks also becomes insufficient for crystal structure refinement at higher *P-T* conditions. Therefore, the crystal structure refinement was reported up to 47.2 GPa, 700 K in run-1 (Fig. 2b). In run-2, only the data at 3.5 GPa were refined, mainly due to the installation of a vacuum enclosure above that pressure, whose SiO_2 glass window affects the intensity of XRD peaks. However, as shown in Figure 3, the peaks of the integrated single-crystal XRD remain sharp and can be used to determine the unit-cell parameters with small uncertainties.

Peak splitting or broadening can be used to detect small structural distortion from cubic prototype to lower-symmetry structure. For powder XRD, however, whether a peak splitting or broadening is due to structural change or non-hydrostatic stress is sometimes difficult to be distinguished. The single-crystal XRD method can distinguish the peaks of degenerated *d*-spacing such as (200) and (002). Thus, if the structural change results in peak splitting/broadening, the *d*-spacing of these two single-crystal spots would deviate; conversely if the non-hydrostatic stress causes peak splitting/broadening, both single-crystal spots would broaden, and their *d*-spacing will remain the same. No splitting of (110), (200), (211) peaks, as mentioned in previous powder and single-crystal XRD measurements (Grande et al. 2022; Kadobayashi et al. 2014; Somayazulu et al. 2008), was observed from our XRD data up to 78.2 GPa, 700 K in run-1 and 31.4 GPa, 1000 K in run-2 (Fig. 3). We also calculated the strain tensors ε11 and ε33 of *a* and *c* axes at 300 K, assuming the indexed (200) and $(\bar{2}00)$ reflections correspond to the *a* axis/ε11, and (002) and $(00\bar{2})$ reflections correspond to the *c* axis/ε33. The reference axial length of the ideal cubic structure was obtained from the average volume calculated using *d*-spacing of these peaks. Up to the highest pressure that we have reached, no obvious change of strain was observed, which means that there is no clear indication of a non-cubic metric from these two axes (Online Materials[1] Fig. S4). However, the information of *b* axis is missing from our data due to the orientation of the synthesized ice-VII crystal, which prevented us from obtaining information on ε22 and searching potential peak splitting between *b* and *a*/*c* axis. At present, a phase transition from cubic to tetragonal structure was not observed based on our data, but the possibility of this transition cannot be ruled out due to the missing axis. We did not observe the kink of the ratio of the intensity of (220)/(110) peaks, which indicates the interstitial proton model above 13 GPa described by Guthrie et al. (2013). Our single-crystal XRD patterns show no obvious evidence for the transition from ice-VII to ice X. This is because ice-VII and ice X have similar *bcc*-type oxygen arrangements, and their differences lie in the hydrogen positions. Since hydrogen scatters X-ray weakly, XRD patterns of ice-VII and ice X are difficult to be distinguished, while Raman, IR, NMR methods, and theoretical calculation may have a better resolution to detect this transition. (Aoki et al. 1996; Goncharov et al. 1999; Grande et al. 2022; Meier et al. 2018; Shi et al. 2021).

In run-2, the ice-VII sample was detected to be molten at 10.9 and 12.5 GPa, 900 K, as indicated by the absence of all single-crystal diffraction peaks (Fig. 2c). The diffraction peaks reappeared at 14.6 GPa, 900 K. The melting point was thus bracketed at 13.6(10) GPa and 900 K. In addition, the diffraction peaks of ice-VII remained at 24.2 GPa, 1000 K (decompression point) and 31.4 GPa, 1000 K, which further constrain the melting curve (Figs. 2d and 4). Due to the fast graphitization of diamond anvils at high temperature, we cannot directly measure the melting point at >20 GPa. Compared with previous studies on melting curve of ice-VII, our results are consistent with the melting curves by Schwager et al. (2004) and Prakapenka et al. (2021), which are the highest among all the melting curves reported in previous studies in this pressure range. The relatively high melting curve of ice-VII would potentially cross the geotherm of some cold water-rich exoplanets and cold subducted slabs in deep Earth (Bina and Navrotsky 2000), supporting the idea of finding ice-VII in the interior of icy cosmic bodies and the Earth.

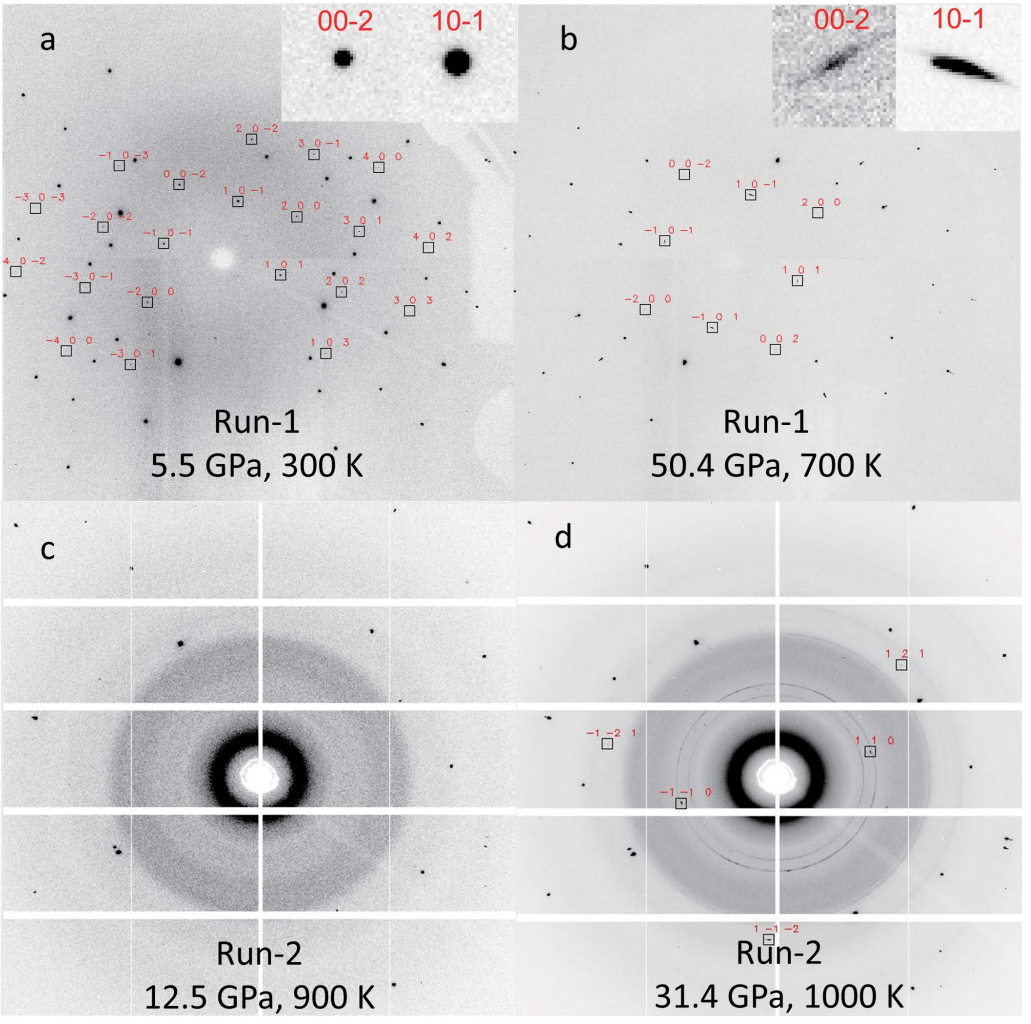

FIGURE 2. Representative XRD patterns of ice-VII and H_2O fluid at high pressures and(or) high temperatures. (**a**) Single-crystal XRD patterns of ice-VII at 5.5 GPa and 300 K in run-1. Inset: enlargement of $(00\bar{2})$ and $(10\bar{1})$ peaks. (**b**) Single-crystal XRD patterns of ice-VII at 50.4 GPa and 700 K in run-1. Inset: enlargement of $(00\bar{2})$ and (101) peaks. (**c**) XRD patterns at 12.5 GPa and 900 K in run-2. Single-crystal diffraction peaks of ice-VII disappeared due to the melting. (**d**) Single-crystal XRD patterns of ice-VII at 31.4 GPa, 1000 K in run-2. Diffraction peaks of the ice-VII were marked by black boxes. Red labels correspond to Miller indices (*hkl*) of the diffraction peaks. Most of other single-crystal peaks are from single-crystal diamond anvils of the EHDAC and several peaks are from impurities outside the sample chamber (Online Materials[1] Fig. S2). The rings in background in **c** and **d** are identified to be the diffraction patterns of the SiO_2 glass of the enclosure and/or Re gasket. (Color online.)

Isothermal equation of state at 300 K

The refined unit-cell parameters of high-pressure ice at 300 K show no obvious volume discontinuity caused by the presumed ice-VII to ice X transition up to the highest pressure investigated, probably due to the subtle and gradual nature of these transitions (Fig. 5a, Online Materials[1] Fig.S5). Normalized stress (F_E) as a function of the Eulerian finite strain (f_E) (*F-f* plot) is plotted in Figure 5b, where $f_E = [(V/V_0)^{-2/3} - 1]/2$ and $F_E = P/[3f_E(1 + 2f_E)^{5/2}]$ and the EoS can be simplified as $F_E = K_0 + 3K_0/2(K_0' - 4)f_E$, neglecting the high-order terms (Angel 2000). Fixed $V_0 = 40.86$ Å^3 and fitted $V_0 = 41.58$ Å^3 were used to calculate the *F-f* plot to see if there are any subtle changes (Fig. 5b; Online Materials[1] Fig. S6). The *F-f* plot also shows no obvious discontinuity over the entire pressure range. In addition, *F-f* plot can be used to verify which order of the B-M EoS is sufficient to satisfactorily represent the compression behavior of the sample (Angel 2000). The quasi-linear *F-f* relationship and the fitted slope close to $3K_0(K' - 4)/2$ suggest the adequacy of using the third-order B-M EoS and the positive slope indicates $K_0' > 4$ (Fig. 5b).

Since there are no indications of discontinuity from our *P-V* data and *F-f* plot, it is reasonable to fit the *P-V* data at 300 K up to 78.2 GPa by single third-order Birch-Murnaghan Equation of State (B-M EoS) and Vinet Equation of State (Vinet EoS). The fittings are weighted by the uncertainties in both pressure and volume (Fig. 5a; Table 1). Since ice-VII is not quenchable at ambient pressure, the zero-pressure volume V_0 of ice-VII has no physical meaning and is less constrained, which only serves as a reference parameter to reproduce the volumes at high pressure. From previous studies, V_0 of ice-VII varies in the fitting of B-M EoS and Vinet EoS (~12.3 cm^3/mol for B-M EoS and ~14.52 cm^3/mol for Vinet EoS except for two giving ~12.1 and ~12.8 cm^3/mol), and sometimes was fixed for comparison (Bezacier et al. 2014; Fei et al. 1993; Frank et al. 2004; Grande et al. 2022; Hemley et al. 1987; Loubeyre et al. 1999; Somayazulu et al. 2008; Sugimura et al. 2008; Wolanin et al. 1997). Here, to fulfill the purpose of better reproducing data and comparing with other studies, we reported EoS parameters by both fitting and fixing zero-pressure volume (Table 1). We also employed

a modified third-order B-M EoS to fit the data using (P_R, V_R) at 3.5 GPa instead of (P_0, V_0) as the starting point.

$$P - P_R = \frac{3K_R}{2}\left[\left(\frac{V_R}{V}\right)^{7/3} - \left(\frac{V_R}{V}\right)^{5/3}\right]\left\{1 + \frac{3}{4}\left(K_R' - 4\right)\left[\left(\frac{V_R}{V}\right)^{2/3} - 1\right]\right\} \quad (1)$$

where P_R is the pressure of the reference point, V_R, K_R, and K_R' are the volume, bulk modulus, and pressure derivative of the reference point.

The fitting parameters obtained from B-M EoS at room temperature in our study are close to those in previous studies (Table 1; Fig. 5a). It is noted that the fitting of Bezacier et al. (2014) deviates from other studies at the high-pressure end because their data coverage is below 10.1 GPa and second-order B-M EoS is used for high-pressure extrapolation. When fitting our data using Vinet EoS with a fixed volume of ~14.52 cm^3/mol, we found that the data at 3.5 GPa is below the fitting curve (Online Materials[1] Fig. S5). The fitting quality is improved when the V_0 was fitted. The fitted V_0 is close to those reported by Wolanin et al. (1997) and Grande et al. (2022), and the K_0 and K_0' agree well with Wolanin et al. (1997). In short, the B-M EoS with fixed and fitted V_0, Vinet EoS with fitted V_0, and modified third-order B-M EoS all give similar and good fitting results to our data (Online Materials[1] Fig. S5).

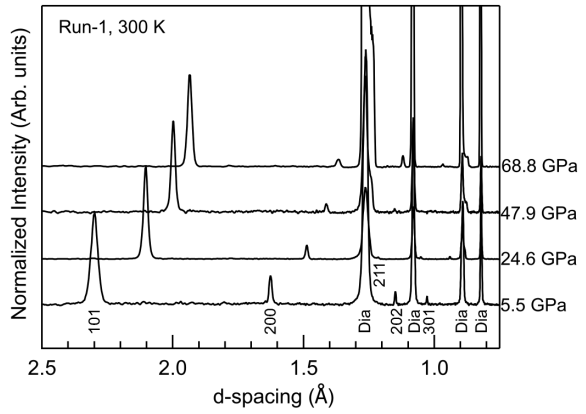

Figure 3. Representative integrated single-crystal XRD patterns at 300 K. The intensity was normalized by the max intensity of ice-VII/ice-VII′/ice X (110) peak. The indexing of XRD peaks of ice-VII and diamond (Dia) from diamond anvils are also shown.

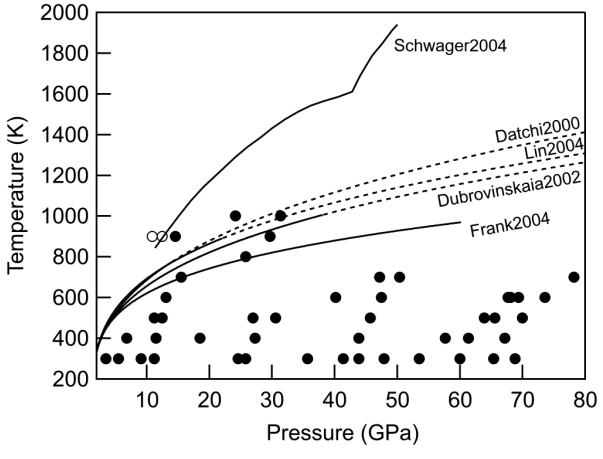

Figure 4. Pressure-temperature conditions of our single-crystal XRD measurements compared with melting curves determined in previous studies (Datchi et al. 2000; Dubrovinskaia and Dubrovinsky 2003; Frank et al. 2004; Lin et al. 2004; Schwager et al. 2004). Solid circle represents the *P-T* conditions at which XRD patterns of high-pressure ice were observed. Open circle represents the *P-T* conditions at which XRD patterns of ice-VII were missing, indicating the melting of ice-VII. The error bars in pressure are within the symbols.

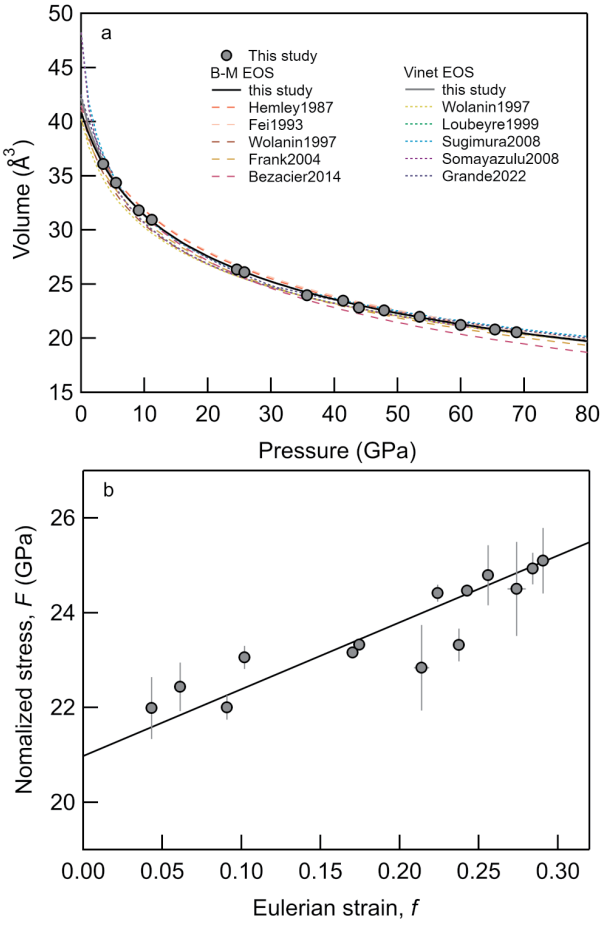

Figure 5. Volume as a function of pressure in this study compared with previous studies and the *F-f* plot of data at 300 K. (**a**) *P-V* data fitted using third-order Birch-Murnaghan EoS [K_0 = 21.0(4) GPa, K_0' = 4.45(6), V_0 = 40.86 Å^3, solid black line] and Vinet EoS [K_0 = 15(2) GPa, K_0' = 5.6(2), V_0 = 42.2(6) Å^3, solid gray line] in our study compared with fittings using third-order Birch-Murnaghan EoS and Vinet EoS in other studies (dashed lines) (Bezacier et al. 2014; Fei et al. 1993; Frank et al. 2004; Grande et al. 2022; Hemley et al. 1987; Loubeyre et al. 1999; Somayazulu et al. 2008; Sugimura et al. 2008; Wolanin et al. 1997). The error bars in pressure and volume are within symbols. (**b**) The *F-f* plot of data at 300 K using the parameters of the third-order B-M EoS with a fixed V_0 in this study. Solid line is the linear fitting. (Color online.)

Thermal equation of state of ice-VII

K_0, K_0', and V_0 were obtained by fitting 300 K data to a third-order B-M EoS as described above. To obtain the thermal

TABLE 1. Thermoelastic properties of ice-VII compared with previous studies

P-T range	K_0 (GPa)	K'	V_0 (cm³/mol)	Thermoelastic parameters	Method	Reference
			BM EoS			
3.5–78.2 GPa, 300–1000 K	21.0 (4)	4.45(6)	12.3 (fixed)	$a_0 = 15(5) \times 10^{-5}$ K^{-1}; $a_1 = 15(8) \times 10^{-8}$ K^{-2}; dK/dT = –0.009(4) GPa/K	SCXRD	This study
3.5–78.2 GPa, 300 K	19.2(15)	4.6(2)	12.4(2)		SCXRD	This study
3.5–78.2 GPa, 300 K	34.3(6)[a]	4.26(7)[a]	10.9[a] (fixed)		SCXRD	This study
4.3–128 GPa, RT	23.7(9)	4.15(7)	12.3(3)		PXRD	Hemley et al. (1987)
6–20 GPa, 300–650 K	23.9(7)	4.2(5)	12.3(2)	$\gamma_0 = 1.2(1)$; $\theta_D = 1470(50)$ K; $q = -2(1)$	PXRD	Fei et al. (1993)
~5–106 GPa, RT	14.9(8) (fixed)	5.4(1)	12.37(8)		PXRD	Wolanin et al. (1997)
6–60 GPa, 850 K	21.1(13)	4.4(1)	12.4(1)	$a_0 = -4.2 \times 10^{-4}$ K^{-1}; $a_1 = 1.56 \times 10^{-6}$ K^{-2};	PXRD	Frank et al. (2004)
2.1–10.1 GPa, 300–450 K	20.15(17)	4(fixed)	12.49(1)	$\eta = 1.1$; $a_0 = 11.58(54) \times 10^{-5}$ K^{-1}	PXRD	Bezacier et al. (2014)
			Vinet EoS			
3.5–78.2 GPa, 300 K	15(2)	5.6(2)	12.7(2)		SCXRD	This study
3.5–78.2 GPa, 300 K	5.4(3)[b]	7.2(2)[b]	14.52[b] (fixed)		SCXRD	This study
~5–106 GPa, RT	14.9(8) (fixed)	6.2(1)	12.1(3)		PXRD	Wolanin et al. (1997)
2–170 GPa, RT	4.26	7.75	14.52		SCXRD	Loubeyre et al. (1999)
16.8–40 GPa, 300K	5.02(43)	7.51(28)	14.52 (fixed)		PXRD	Sugimura et al. (2008)
10–120 GPa	5.10(20)	7.50(12)	14.52(fixed)		Theoretical	Sugimura et al. (2008)
3–48 GPa, RT	4.21(4)	7.77(2)	14.52(5)		PXRD, rXRD, SXRD	Somayazulu et al. (2008)
19–50 GPa, 300–873 K	5.02	7.51	14.52 (fixed)	$\alpha_0 = 150(19) \times 10^{-5}$ K^{-1}; $\delta_T = 5.1(2)$	PXRD	Sugimura et al. (2010)
2.7–5.1 GPa, RT	18.5(40)	2.5(16)	12.79(27)		PXRD	Grande et al. (2022)
5.1–30.9 GPa, RT	20.8(25)	4.49(35)	12.37(16)		PXRD	Grande et al. (2022)
30.9–60 GPa, RT	50.5(42)	4.50(15)	10.18(13)		PXRD	Grande et al. (2022)

Notes: SCXRD and PXRD are acronyms of single-crystal XRD and powder XRD.
[a] Parameters are obtained by a modified third-order B-M EoS.
[b] Fixed volume for better comparison with other studies, while the data at 3.5 GPa is below the fitting curve, suggesting that our Vinet EoS fitting results with the volume not fixed is better.

expansion α_T and dK/dT, high *P-T* data at 400, 500, 600, 700, 800, 900, and 1000 K were together fitted by a high-temperature Birch-Murnaghan EoS (Berman 1988) (Fig. 6). Assuming that dK/dT is constant through the fitted temperature ranges, K_{T0} and K'_{T0} can be described as:

$$K_{T0} = K_0 + dK/dT \times (T - 300) \quad (2)$$
$$K'_{T0} = K'_0 \quad (3)$$

and the temperature dependence of volume can be expressed by the empirical polynomial equation (Berman 1988) as:

$$V_{T0} = V_0[1 + \alpha_0(T - 300)] + \tfrac{1}{2}\alpha_1[T - 300)^2]. \quad (4)$$

Taking the first derivative of Equation 3 gives the thermal expansion coefficient $\alpha_T = \alpha_0 + \alpha_1(T - 300)$ by approximation. The fit to the *P-V-T* data (Online Materials[1] Table S1) gives dK/dT = –0.009(4) GPa/K and thermal expansion $\alpha_T = 15(5) \times 10^{-5} + 15(8) \times 10^{-8} \times (T - 300)$ K^{-1}.

It is difficult to compare the parameters of thermal EoS because several different thermal EoSs were used in previous studies (Table 1). Thus, we plot the original data from previous studies for comparison (Fig. 6). For showing temperatures in different studies, a continuous colored scale was used. From the color consistency, the high-temperature data and fitted thermal EoS from our study are overall in good agreement with the ones in other studies. High-temperature volumes relative to the volume at 300 K are plotted in the inset of Figure 6, and the pressure residuals of the fitting are plotted in Figure 6, which both show that our experimental data are well reproduced by the fitted thermal EoS. The pressure and temperature range of the thermal EoS in this study is extended compared with previous studies, especially for the temperature points higher than 800 K, due to the usage of vacuum enclosure on EHDAC. The wider temperature and pressure coverage will provide better constraints on thermal expansion and elasticity for calculation and modeling.

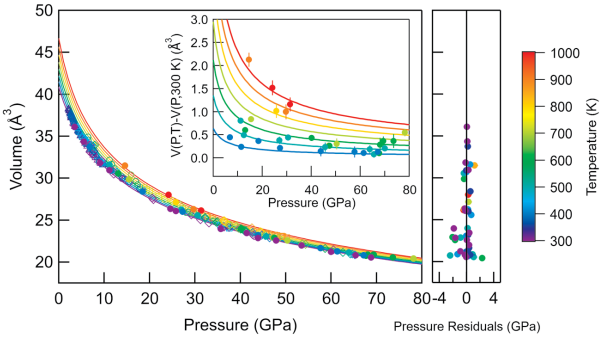

FIGURE 6. Volumes of high-pressure ice at high pressures and high temperatures. The pressure and volume uncertainties are shown by the horizontal and vertical error bars. The isothermal curves at 300–1000 K with a step of 100 K are calculated by the high-temperature Birch-Murnaghan EoS in this study. Solid circles represent the data in this study. The hollow circles, diamonds, squares, and triangles represent data from (Bezacier et al. 2014; Fei et al. 1993; Frank et al. 2004; Sugimura et al. 2010), respectively. Pressure residuals are shown on the right side of the figure. The error bars in pressure and volume are within symbols. Inset: Volumes relative to the volume at 300 K. The volumes at 300 K are calculated by the Birch-Murnaghan EoS in this study. (Color online.)

GEOPHYSICAL IMPLICATIONS

Ice-VII phase may be present in various planetary environments, especially in the interiors of icy planets or satellites. The ice shell of these planets or satellites, if reaching a pressure higher than 2.1 GPa, will stabilize ice-VII (temperature >~293 K) or ice VIII (temperature <~293 K) as its major phase. Therefore, ice-VII was proposed to widely exist in icy bodies such as Titan, Gliese 436b, and GJ1214b, whose sizes are relatively large. Ganymede has a ~800–900 km icy shell, and the boundary pressure of icy shell and mantle is around 1.7–2.2 GPa depending on the model (Kronrod and Kuskov 2006; Kuskov and Kronrod 2001); therefore, whether or not a thin ice-VII layer can exist is still unclear.

Modeling the internal structures of these icy bodies requires the density data of the phases in each layer to fit the moment of inertia, and the pressure-density data of high-pressure ices like ice-VII are essential for the modeling, especially for those larger icy bodies. For example, the homogeneous model of Ganymede and Titan in an earlier study used the EoS of ice-VII (Lupo 1982). It is noted that the internal temperatures of these icy bodies are highly uncertain, e.g., the highest temperature of Ganymede was estimated at around 300 K in the study of Lupo (1982), while in the study of Kronrod and Kuskov (2006), the temperature at the ice-silicate boundary was around 800 K. Therefore, the thermal EoS determined in this study could provide better constraints for those different models.

Ice-VII is a newly named mineral after its discovery in superdeep diamond inclusions (Tschauner et al. 2018). Ice-VII inclusions, although rare, provide direct evidence of the depths that the deep water cycle can reach and the formation environment of host diamonds. The thermal EoS of ice-VII reported in this study, together with the thermal EoS of H_2O fluid and diamond, are the key parameters for the determination of the originated depth and temperature of the ice-VII inclusions of diamonds originated from the deep mantle (Tschauner et al. 2018; Wang et al. 2021). We recalculated the isomeke *P-T* paths of superdeep diamond GRR1507 and M57666 reported by Tschauner et al. (2018) utilizing the thermal EoS parameters of ice-VII and diamond from this study and Angel et al. (2015), respectively. The remanent pressures of ice-VII inclusions for calculation were 7.9 and 9.2 GPa for GRR1507 and M57666, respectively. The calculated *P-T* paths mostly fall in the range of the *P-T* paths by Wang et al. (2021) based on first-principle calculation, with a slightly steeper slope (Fig. 7). It indicates that the thermoelastic parameters by this study and the theoretical calculation are consistent with each other and those parameters can be used for the calculation of entrapment pressure of H_2O in superdeep diamond.

The discovery of ice-VII also makes it a potential mineral phase in the deep mantle. Since pure H_2O can easily react with dry silicates to form hydrous phases, ice-VII is not likely to be a global water host in the mantle. It could only be stabilized within extremely water-rich regions, such as the several dehydration zones of the coldest slabs. The seismic anomaly induced by ice-VII, if any, would thus be interfered by the presence of the complex mineral and fluid products from dehydration and is not likely to be visible during the seismic detection.

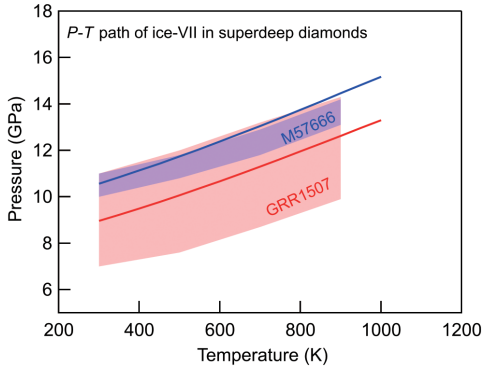

Figure 7. Isomeke *P-T* paths of ice-VII in superdeep diamonds calculated using thermoelastic properties of ice-VII in this study compared with a previous study (Wang et al. 2021). (Color online.)

Acknowledgments

We thank Stella Chariton and Wenzhong Wang for the valuable discussion, editor Tschauner and two anonymous reviewers for their constructive comments. We also would like to thank Sinogeikin Stas (DAC Tools company) for the help with EHDAC development.

Funding

X. Lai acknowledges support from the Fundamental Research Funds for the Central Universities, China University of Geosciences (Wuhan) (no.162301202618) and National Natural Science Foundation of China grant (no. 42002041). F. Zhu acknowledges support from National Natural Science Foundation of China grant (no. 42102035). B. Chen acknowledges support from the U.S. National Science Foundation (NSF) (EAR-1555388 and EAR-1829273). This research used resources of the Advanced Photon Source (APS), a U.S. Department of Energy (DOE) Office of Science User Facility operated for the DOE Office of Science by Argonne National Laboratory under Contract No. DE-AC02-06CH11357. We acknowledge the support of GeoSoilEnviroCARS (Sector 13), which is supported by National Science Foundation(NSF)-Earth Sciences (EAR-1634415). The development of EHDAC was supported by Externally heated Diamond Anvil Cell Experimentation (EH-DANCE) project to B. Chen under Education Outreach and Infrastructure Development (EOID) project from COMPRES under NSF Cooperative Agreement EAR-1606856.

References cited

Angel, R.J. (2000) Equations of state. Reviews in Mineralogy and Geochemistry, 41, 35–59, https://doi.org/10.2138/rmg.2000.41.2.

Angel, R., Alvaro, M., Nestola, F., and Mazzucchelli, M. (2015) Diamond thermoelastic properties and implications for determining the pressure of formation of diamond-inclusion systems. Russian Geology and Geophysics, 56, 211–220, https://doi.org/10.1016/j.rgg.2015.01.014.

Angel, R.J., Mazzucchelli, M.L., Alvaro, M., and Nestola, F. (2017) EosFit-Pinc: A simple GUI for host-inclusion elastic thermobarometry. American Mineralogist, 102, 1957–1960, https://doi.org/10.2138/am-2017-6190.

Aoki, K., Yamawaki, H., Sakashita, M., and Fujihisa, H. (1996) Infrared absorption study of the hydrogen-bond symmetrization in ice to 110 GPa. Physical Review B: Condensed Matter, 54, 15673–15677, https://doi.org/10.1103/PhysRevB.54.15673.

Asahara, Y., Hirose, K., Ohishi, Y., Hirao, N., and Murakami, M. (2010) Thermoelastic properties of ice VII and its high-pressure polymorphs: Implications for dynamics of cold slab subduction in the lower mantle. Earth and Planetary Science Letters, 299, 474–482, https://doi.org/10.1016/j.epsl.2010.09.037.

Berman, R.G. (1988) Internally-consistent thermodynamic data for minerals in the system Na_2O–K_2O-CaO-MgO-FeO-Fe_2O_3-Al_2O_3-SiO_2-TiO_2–H_2O-CO_2. Journal of Petrology, 29, 445–522, https://doi.org/10.1093/petrology/29.2.445.

Bezacier, L., Journaux, B., Perrillat, J.-P., Cardon, H., Hanfland, M., and Daniel, I. (2014) Equations of state of ice VI and ice VII at high pressure and high temperature. The Journal of Chemical Physics, 141, 104505, https://doi.org/10.1063/1.4894421.

Bina, C.R. and Navrotsky, A. (2000) Possible presence of high-pressure ice in cold subducting slabs. Nature, 408, 844–847, https://doi.org/10.1038/35048555.

Bridgman, P.W. (1937) The phase diagram of water to 45,000 kg/cm^2. The Journal of Chemical Physics, 5, 964–966, https://doi.org/10.1063/1.1749971.

Brown, A. and Whalley, E. (1966) Preliminary investigation of the phase boundaries between ice VI and VII and ice VI and VIII. The Journal of Chemical Physics, 45, 4360–4361, https://doi.org/10.1063/1.1727503.

Datchi, F., Loubeyre, P., and LeToullec, R. (2000) Extended and accurate determination of the melting curves of argon, helium, ice (H_2O), and hydrogen (H_2). Physical Review B: Condensed Matter, 61, 6535–6546, https://doi.org/10.1103/PhysRevB.61.6535.

Dera, P., Zhuravlev, K., Prakapenka, V., Rivers, M.L., Finkelstein, G.J., Grubor-Urosevic, O., Tschauner, O., Clark, S.M., and Downs, R.T. (2013) High pressure single-crystal micro X-ray diffraction analysis with GSE_ADA/RSV software. High Pressure Research, 33, 466–484, https://doi.org/10.1080/08957959.2013.806504.

Dolomanov, O.V., Bourhis, L.J., Gildea, R.J., Howard, J.A., and Puschmann, H. (2009) OLEX2: A complete structure solution, refinement and analysis program. Journal of Applied Crystallography, 42, 339–341, https://doi.org/10.1107/S0021889808042726.

Dubrovinskaia, N. and Dubrovinsky, L. (2003) Melting curve of water studied in externally heated diamond-anvil cell. High Pressure Research, 23, 307–311, https://doi.org/10.1080/0895795031000139226.

Fei, Y., Mao, H., and Hemley, R.J. (1993) Thermal expansivity, bulk modulus, and melting curve of H_2O–ice VII to 20 GPa. The Journal of Chemical Physics, 99, 5369–5373, https://doi.org/10.1063/1.465980.

Fei, Y., Ricolleau, A., Frank, M., Mibe, K., Shen, G., and Prakapenka, V. (2007) Toward an internally consistent pressure scale. Proceedings of the National Academy of Sciences, 104, 9182–9186, https://doi.org/10.1073/pnas.0609013104.

Frank, M.R., Fei, Y., and Hu, J. (2004) Constraining the equation of state of fluid H_2O to 80 GPa using the melting curve, bulk modulus, and thermal expansivity of ice VII. Geochimica et Cosmochimica Acta, 68, 2781–2790, https://doi.org/10.1016/j.gca.2003.12.007.

Futera, Z., Tse, J.S., and English, N.J. (2020) Possibility of realizing superionic ice VII in external electric fields of planetary bodies. Science Advances, 6, eaaz2915, https://doi.org/10.1126/sciadv.aaz2915.

Goncharov, A.F., Struzhkin, V.V., Mao, H., and Hemley, R.J. (1999) Raman spectroscopy of dense H_2O and the transition to symmetric hydrogen bonds. Physical Review Letters, 83, 1998–2001, https://doi.org/10.1103/PhysRevLett.83.1998.

Gonzalez-Platas, J., Alvaro, M., Nestola, F., and Angel, R. (2016) EosFit7-GUI: A new graphical user interface for equation of state calculations, analyses and teaching. Journal of Applied Crystallography, 49, 1377–1382, https://doi.org/10.1107/S1600576716008050.

Grande, Z.M., Pham, C.H., Smith, D., Boisvert, J.H., Huang, C., Smith, J.S., Goldman, N., Belof, J.L., Tschauner, O., Steffen, J.H., and others. (2022) Pressure-driven symmetry transitions in dense H_2O ice. Physical Review B, 105, 104109, https://doi.org/10.1103/PhysRevB.105.104109.

Guthrie, M., Boehler, R., Tulk, C.A., Molaison, J.J., dos Santos, A.M., Li, K., and Hemley, R.J. (2013) Neutron diffraction observations of interstitial protons in dense ice. Proceedings of the National Academy of Sciences, 110, 10552–10556, https://doi.org/10.1073/pnas.1309277110.

Hemley, R., Jephcoat, A., Mao, H., Zha, C., Finger, L., and Cox, D. (1987) Static compression of H_2O-ice to 128 GPa (1.28 Mbar). Nature, 330, 737–740, https://doi.org/10.1038/330737a0.

Huang, C., Rice, D.R., Grande, Z.M., Smith, D., Smith, J.S., Boisvert, J.H., Tschauner, O., Salamat, A., and Steffen, J.H. (2021) Implications of an improved water equation of state for water-rich planets. Monthly Notices of the Royal Astronomical Society, 503, 2825–2832, https://doi.org/10.1093/mnras/stab645.

Iitaka, T., Fukui, H., Li, Z., Hiraoka, N., and Irifune, T. (2015) Pressure-induced dissociation of water molecules in ice VII. Scientific Reports, 5, 12551, https://doi.org/10.1038/srep12551.

Kadobayashi, H., Hirai, H., Matsuoka, T., Ohishi, Y., and Yamamoto, Y. (2014) A possible existence of phase change of deuterated ice VII at about 11 GPa by X-ray and Raman studies. Journal of Physics: Conference Series, 500, 182017, https://doi.org/10.1088/1742-6596/500/18/182017.

Kamb, B. and Davis, B.L. (1964) Ice VII, the densest form of ice. Proceedings of the National Academy of Sciences, 52, 1433–1439, https://doi.org/10.1073/pnas.52.6.1433.

Kantor, I., Prakapenka, V., Kantor, A., Dera, P., Kurnosov, A., Sinogeikin, S., Dubrovinskaia, N., and Dubrovinsky, L. (2012) BX90: A new diamond anvil cell design for X-ray diffraction and optical measurements. The Review of Scientific Instruments, 83, 125102, https://doi.org/10.1063/1.4768541.

Kronrod, V. and Kuskov, O. (2006) Chemical differentiation of the Galilean satellites of Jupiter: 4. Isochemical models for the compositions of Io, Europa, and Ganymede. Geochemistry International, 44, 529–546, https://doi.org/10.1134/S0016702906060012.

Kuhs, W., Finney, J., Vettier, C., and Bliss, D. (1984) Structure and hydrogen ordering in ices VI, VII, and VIII by neutron powder diffraction. The Journal of Chemical Physics, 81, 3612–3623, https://doi.org/10.1063/1.448109.

Kuskov, O.L. and Kronrod, V.A. (2001) Core sizes and internal structure of Earth's and Jupiter's satellites. Icarus, 151, 204–227, https://doi.org/10.1006/icar.2001.6611.

Lai, X., Zhu, F., Zhang, J.S., Zhang, D., Tkachev, S., Prakapenka, V.B., and Chen, B. (2020) An externally-heated diamond anvil cell for synthesis and single-crystal elasticity determination of ice-VII at high pressure-temperature conditions. Journal of Visualized Experiments, 160, e61389.

Li, X., Shi, W., Liu, X., and Mao, Z. (2019) High-pressure phase stability and elasticity of ammonia hydrate. American Mineralogist. Journal of Earth and Planetary Materials, 104, 1307–1314.

Lin, J.-F., Militzer, B., Struzhkin, V.V., Gregoryanz, E., Hemley, R.J., and Mao, H.K. (2004) High pressure-temperature Raman measurements of H_2O melting to 22 GPa and 900 K. The Journal of Chemical Physics, 121, 8423–8427, https://doi.org/10.1063/1.1784438.

Loubeyre, P., LeToullec, R., Wolanin, E., Hanfland, M., and Hausermann, D. (1999) Modulated phases and proton centering in ice observed by X-ray diffraction up to 170? GPa. Nature, 397, 503–506, https://doi.org/10.1038/17300.

Lupo, M.J. (1982) Mass-radius relationships in icy satellites after Voyager. Icarus, 52, 40–53, https://doi.org/10.1016/0019-1035(82)90167-1.

Mao, H., Xu, J.-A., and Bell, P. (1986) Calibration of the ruby pressure gauge to 800 kbar under quasi-hydrostatic conditions. Journal of Geophysical Research, 91 (B5), 4673–4676, https://doi.org/10.1029/JB091iB05p04673.

Meier, T., Petitgirard, S., Khandarkhaeva, S., and Dubrovinsky, L. (2018) Observation of nuclear quantum effects and hydrogen bond symmetrisation in high pressure ice. Nature Communications, 9, 2766, https://doi.org/10.1038/s41467-018-05164-x.

Poirier, J., Sotin, C., and Peyronneau, J. (1981) Viscosity of high-pressure ice VI and evolution and dynamics of Ganymede. Nature, 292, 225–227, https://doi.org/10.1038/292225a0.

Prakapenka, V.B., Holtgrewe, N., Lobanov, S.S., and Goncharov, A.F. (2021) Structure and properties of two superionic ice phases. Nature Physics, 17, 1233–1238, https://doi.org/10.1038/s41567-021-01351-8.

Prescher, C. and Prakapenka, V.B. (2015) DIOPTAS: A program for reduction of two-dimensional X-ray diffraction data and data exploration. High Pressure Research, 35, 223–230, https://doi.org/10.1080/08957959.2015.1059835.

Schwager, B., Chudinovskikh, L., Gavriliuk, A., and Boehler, R. (2004) Melting curve of H_2O to 90 GPa measured in a laser-heated diamond cell. Journal of Physics Condensed Matter, 16, S1177–S1179, https://doi.org/10.1088/0953-8984/16/14/028.

Seager, S., Kuchner, M., Hier-Majumder, C., and Militzer, B. (2007) Mass-radius relationships for solid exoplanets. The Astrophysical Journal, 669, 1279–1297, https://doi.org/10.1086/521346.

Seto, Y. (2010) Development of a software suite on X-ray diffraction experiments. The Review of High Pressure Science and Technology, 20, 269–276.

Shi, W., Sun, N., Li, X., Mao, Z., Liu, J., and Prakapenka, V.B. (2021) Single-crystal elasticity of high-pressure ice up to 98 GPa by Brillouin scattering. Geophysical Research Letters, 48(8), e2021GL092514.

Sohl, F., Spohn, T., Breuer, D., and Nagel, K. (2002) Implications from Galileo observations on the interior structure and chemistry of the Galilean satellites. Icarus, 157, 104–119, https://doi.org/10.1006/icar.2002.6828.

Somayazulu, M., Shu, J., Zha, C.S., Goncharov, A.F., Tschauner, O., Mao, H.K., and Hemley, R.J. (2008) In situ high-pressure X-ray diffraction study of H_2O ice VII. The Journal of Chemical Physics, 128, 064510, https://doi.org/10.1063/1.2813890.

Song, M., Yamawaki, H., Fujihisa, H., Sakashita, M., and Aoki, K. (1999) Infrared absorption study of Fermi resonance and hydrogen-bond symmetrization of ice up to 141 GPa. Physical Review B: Condensed Matter, 60, 12644–12650, https://doi.org/10.1103/PhysRevB.60.12644.

Sugimura, E., Iitaka, T., Hirose, K., Kawamura, K., Sata, N., and Ohishi, Y. (2008) Compression of H_2O ice to 126 GPa and implications for hydrogen-bond symmetrization: Synchrotron X-ray diffraction measurements and density-functional calculations. Physical Review B: Condensed Matter and Materials Physics, 77, 214103, https://doi.org/10.1103/PhysRevB.77.214103.

Sugimura, E., Komabayashi, T., Hirose, K., Sata, N., Ohishi, Y., and Dubrovinsky, L.S. (2010) Simultaneous high-pressure and high-temperature volume measurements of ice VII and its thermal equation of state. Physical Review B: Condensed Matter and Materials Physics, 82, 134103, https://doi.org/10.1103/PhysRevB.82.134103.

Tobie, G., Grasset, O., Lunine, J.I., Mocquet, A., and Sotin, C. (2005) Titan's internal structure inferred from a coupled thermal-orbital model. Icarus, 175, 496–502, https://doi.org/10.1016/j.icarus.2004.12.007.

Tschauner, O., Huang, S., Greenberg, E., Prakapenka, V.B., Ma, C., Rossman, G.R., Shen, A.H., Zhang, D., Newville, M., Lanzirotti, A., and others. (2018) ice-VII inclusions in diamonds: Evidence for aqueous fluid in Earth's deep mantle. Science, 359, 1136–1139, https://doi.org/10.1126/science.aao3030.

Wang, W., Tschauner, O., Huang, S., Wu, Z., Meng, Y., Bechtel, H., and Mao, H.-K. (2021) Coupled deep-mantle carbon-water cycle: Evidence from lower-mantle diamonds. The Innovation, 2, 100117, https://doi.org/10.1016/j.xinn.2021.100117.

Wolanin, E., Pruzan, P., Chervin, J., Canny, B., Gauthier, M., Häusermann, D., and Hanfland, M. (1997) Equation of state of ice VII up to 106 GPa. Physical Review B: Condensed Matter, 56, 5781–5785, https://doi.org/10.1103/PhysRevB.56.5781.

Manuscript received April 17, 2022
Manuscript accepted September 21, 2022
Accepted manuscript online September 29, 2022
Manuscript handled by Oliver Tschauner

Endnote:

[1]Deposit item AM-23-88554, Online Materials. Deposit items are free to all readers and found on the MSA website, via the specific issue's Table of Contents (go to http://www.minsocam.org/MSA/AmMin/TOC/2023/Aug2023_data/Aug2023_data.html). The CIF has been peer-reviewed by our Technical Editors.